



ROBOTICS PROJECT I
Semester project

Prediction of ground reaction forces and moments

Artur JESSLEN

Supervised by:
Dr. STANEV Dimitar

Professor:
Pr. IJSPEERT Auke

ACADEMIC YEAR 2019-2020
Spring semester - 10 ECTS credits

JUNE 22, 2020

Contents

1	Introduction	2
2	Background	3
2.1	Model 1: <i>Skals et al.</i>	3
2.1.1	Musculoskeletal model	3
2.1.2	Prediction of GRF&M	4
2.2	Model 2: <i>Ryu et al.</i>	5
2.3	Model 3: <i>Krüger et al.</i>	7
2.3.1	Contact model	7
2.3.2	Optimization problem	7
2.4	Model 4: <i>Geijtenbeek et al.</i>	9
2.4.1	Muskoskeletal model	9
2.4.2	Method of prediction	10
2.5	Model 5: <i>Karatsidis</i>	11
3	Implemented models	13
3.1	Experimental protocol	13
3.2	Data processing	14
3.3	Data analysis	14
3.3.1	Implemented model 1	14
3.3.2	Implemented model 2	15
3.3.3	Final implementation	16
4	Results	20
5	Discussion	26
Appendices		28
A	Abbreviations	28
B	Complementary figures	28

1 Introduction

The estimation of ground reactions force and moment (GRF&M) is an important stage in biomechanical analysis procedures.

Generally, these measures are recorded using force plate (FP) systems, which despite their high accuracy, have several significant limitations. Firstly, due to their high cost, most laboratories are equipped with one or a couple of FPs, which makes the tracking of many successive steps during overground walking impossible. Moreover, the fixed position of these plates on the ground together with the requirement to step with the whole foot on the plate for a successful measurement may cause subjects to alter their natural gait pattern.

Recent advances in biomechanical analysis techniques are allowing the estimation of GRF&M using only kinematics data. When applied to gait analysis, a common problem that needs to be addressed is the distribution of the total external force and moment during periods of double foot support.

To apply kinetics prediction methods to kinematic data, most of the existing research uses optical motion capture (OMC). However, the increased accuracy and reduced size, power and cost of IMUs have enabled the assessment of segment orientation and later full-body motion capture in laboratory-free settings. This technique delivers good accuracy in estimating human body kinematics, such as joint angles, and has been previously validated versus optical motion capture estimations.

2 Background

2.1 Model 1: *Skals et al.*

The first model has been developed by Sebastian Laigaard Skals for his master's thesis^[1]. It resulted in a paper^[2] which was published one year after (2016) in Springer. In this section, we will describe this model.

2.1.1 Musculoskeletal model

The musculoskeletal models were developed in the AnyBody Modeling System v. 6.0.4 (AMS) based on the GaitFullBody template (Fig. 1).

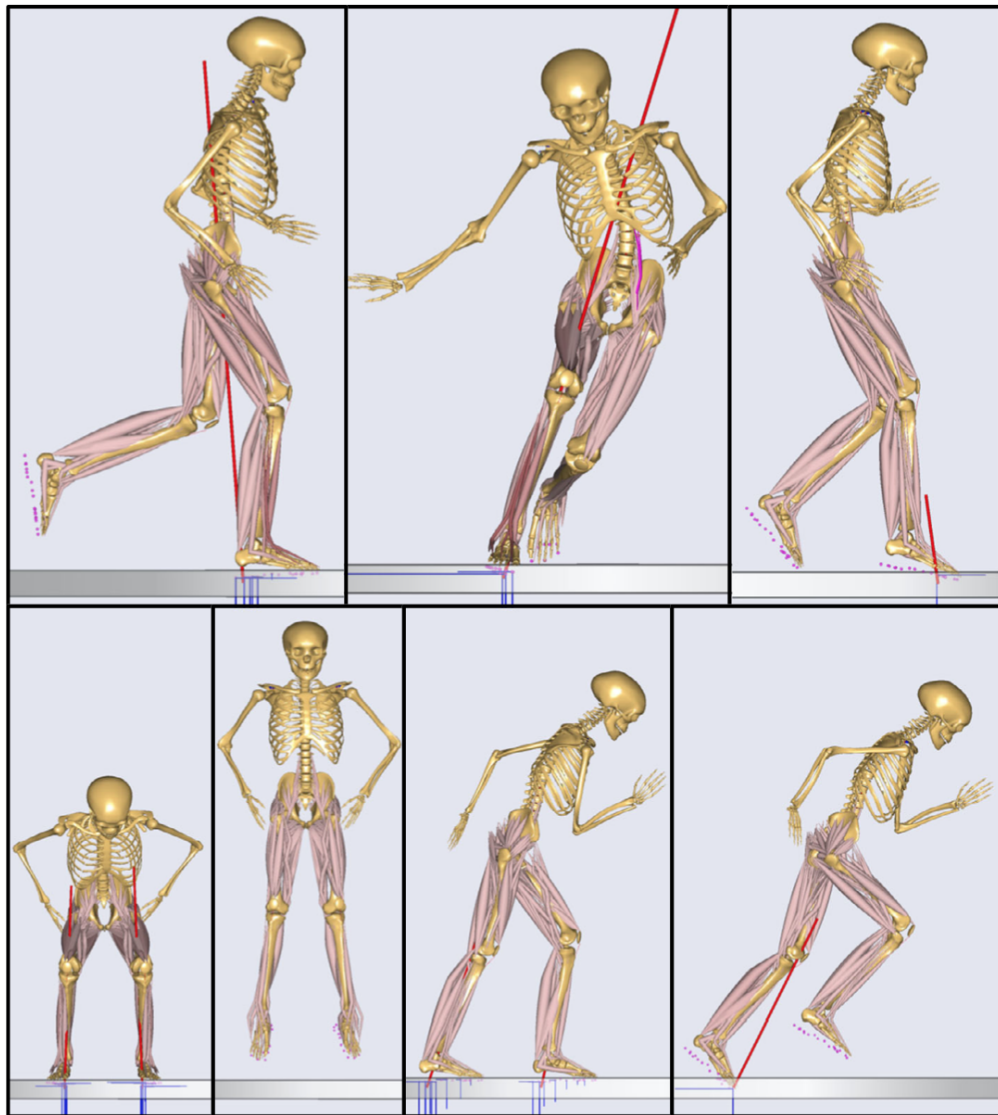


Figure 1: Model used by Skals et al. From top left to bottom right: musculoskeletal models during running, the side-cut maneuver, backward running, vertical jump (counter-movement and past toe-off), and acceleration from a standing position (initiation of the movement and near toe-off).

A length-mass scaling law [3] was applied to scale the musculoskeletal models to the different sizes of the subjects. The inertial parameters were estimated by assuming that the segments were cylindrical with a uniform density and length and mass equal to the segment length and mass. The muscle recruitment problem was solved by formulating a quadratic optimization problem that minimizes an objective function G (eq. 1) where we ensure that muscles can only pull and each unilateral contact element $f_i^{(C)}$ and pelvis residual force $f_i^{(R)}$ can only push.

$$\min_f G(\mathbf{f}^M) = \sum_{i=1}^{n^{(M)}} \left(\frac{f_i^{(M)}}{N_i^{(M)}} \right)^2 + \sum_{i=1}^{5n^{(C)}} \left(\frac{f_i^{(C)}}{N_i^{(C)}} \right)^2 + \sum_{i=1}^{n^{(R)}} \left(\frac{f_i^{(R)}}{N_i^{(R)}} \right)^2 \quad (1)$$

$\mathbf{C}\mathbf{f} = \mathbf{d}$

where $f_i^{(M)}$ is the i^{th} muscle force, $n^{(M)}$ is the number of muscles, $N_i^{(M)}$ is the strength of the muscle, $f_i^{(C)}$ is the i^{th} contact force, $n^{(C)}$ is the number of contact elements, $N_i^{(C)}$ is the strength of the contact element, $f_i^{(R)}$ is the i^{th} residual force, $n^{(R)}$ is the number of residual forces, $N_i^{(R)}$ is the strength of the residual forces. \mathbf{C} is the coefficient matrix for the dynamic equilibrium equations, \mathbf{f} is a vector of unknown muscle, joint reaction, contact and residual forces and \mathbf{d} contains all external loads and inertia forces.

2.1.2 Prediction of GRF&M

In this model, the GRF&Ms were predicted by creating contact elements at 18 points defined under each foot of the musculoskeletal model (Fig. 2).

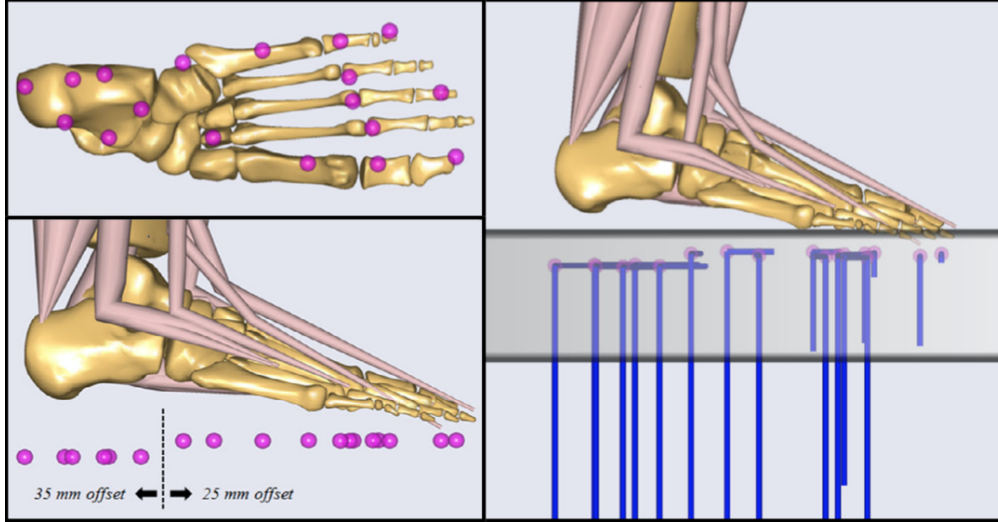


Figure 2: Location of the contact points under the foot of the musculoskeletal model (*top left*), side-view of the contact points illustrating the offset distances (*bottom left*) and the point activation after established ground contact (*right*).

In order to compensate for the sole thickness of the running shoes and the soft tissue under the heel, the contact points on the heel were offset by 35 mm, and all other points offset by 25 mm from the model bone geometry. Each contact element consisted of five

unilateral force actuators organized to approximate a static Coulomb friction model. One actuator was aligned with the vertical axis of the force plates (z-axis) and generated a normal force, whereas the other four actuators were gathered in pairs that were aligned with the medio-lateral (x-axis) and antero-posterior axis (y-axis) of the force plates, and were able to generate positive and negative static friction forces (with a friction coefficient of 0.5). The four shear actuators were organized to independently generate a force in the normal direction and in one of the four shear directions (positive/negative medial-lateral direction or positive/negative antero-posterior direction). For each of these four actuators, the forces were defined such that if they were actuated to generate a force F_n in the normal direction, they would at the same time generate a force of μF_n in the shear direction, where μ is the friction coefficient. Hereby, the total normal force at a contact point is equal to the sum of the five normal forces, and the magnitude of the friction force is bounded by the normal force.

To accommodate the fact that there can only be contact forces at the contact points when they are close to the ground plane and stationary, a strength factor, similar to the one used for muscles, was introduced. Additionally, the magnitudes of the predicted GRF&Ms were determined by solving the activation level of muscle, joint, and ground contact forces as part of the muscle recruitment algorithm simultaneously. To determine the strength profile of each contact point, a nonlinear strength function was defined:

$$c_{p,i} = \begin{cases} N_{max} & \text{if } z_{ratio} \leq 0.8 \text{ and } \nu_{ratio} \leq 0.15, \\ N_{smooth} & \text{if } 0.8 < z_{ratio} \leq 1 \text{ and } 0.15 < \nu_{ratio} \leq 1 \\ 0 & \text{otherwise,} \end{cases} \quad (2)$$

where

$$z_{ratio} = \frac{p_z}{p_{limit}} \text{ and } \nu_{ratio} = \frac{p_{vel}}{\nu_{limit}}$$

p_z and p_{vel} define the height and velocity of each contact point relative to the ground

$$N_{smooth} = N_{max} \nu_{smooth} z_{smooth} \quad (3)$$

where

$$z_{smooth} = 0.5 \left(\cos \left(\frac{z_{ratio} - 0.8}{(1 - 0.8)\pi} \right) + 1 \right) \text{ and } \nu_{smooth} = 0.5 \left(\cos \left(\frac{\nu_{ratio} - 0.15}{(1 - 0.15)\pi} \right) + 1 \right)$$

Finally, the solver did not distinguish between single and double-support phases, hereby, providing a solution to the problem of underdeterminacy.

2.2 Model 2: Ryu et al.

The paper^[5] written by H. X. Ryu and S. Park in Journal of biomechanics in 2018 presents a simple model to estimate unmeasured ground reaction forces based on the oscillatory characteristics of the center of mass (CoM).

This model will not be developed extensively as it is not as valuable as the others.

The model consists of a mass and a spring that respectively represent the CoM and effective lower-limb stiffness of a human. In this model, GRFs are represented by the spring resistance forces of the springy leg, which are calculated by multiplying the stiffness k and the length change of the springy leg, $\Delta l = l - l_0$, where l and l_0 are the current and initial leg lengths. The pivot point was translated to represent the CoP translation from heel to toe during stance phases.

The springy walking model generates infinitely many solutions. Among those solutions, a solution that minimized an objective function was selected. They defined two objective functions depending on the available measurement data. When vertical GRF data was available, an objective function was defined as the sum of the squared residual between the data and the model simulation (eq. 4). When vertical GRF was not measured, they defined the objective function in an alternative way (eq. 5).

$$J = \sum_{i=0}^{100} (GRF_{z,data}[i] - GRF_{z,sim}[i])^2 \quad (4)$$

or

$$\begin{aligned} J &= J_{height} + J_{vel_x} + J_{vel_z} \\ &= \frac{(z_{HS,2} - z_{HS,1})^2 + (z_{TO,2} - z_{TO,1})^2}{l_0^2} \\ &\quad + \frac{(\dot{x}_{HS,2} - \dot{x}_{HS,1})^2 + (\dot{x}_{TO,1} - \dot{x}_{HS,1})^2 + (\dot{x}_{TO,2} - \dot{x}_{HS,1})^2}{\bar{v}^2} \\ &\quad + \frac{(\dot{z}_{HS,2} - \dot{z}_{HS,1})^2 + (-\dot{z}_{TO,1} - \dot{z}_{HS,1})^2 + (-\dot{z}_{TO,2} - \dot{z}_{HS,1})^2}{\bar{v}^2} \end{aligned} \quad (5)$$

with HS meaning "Heel Strike" and TO "Toes Off".

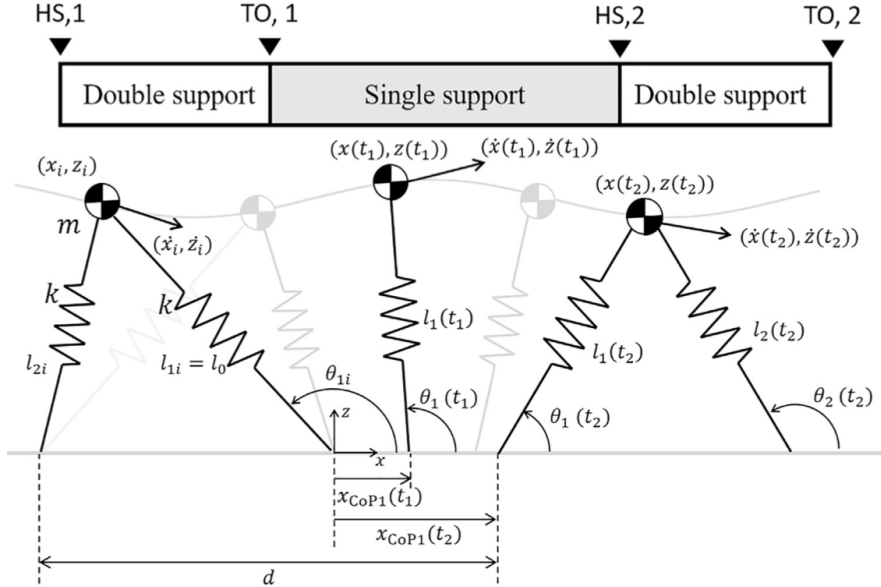


Figure 3: Model details for each gait phase of the simulation..

The main limitations for this model is that it assumes that the dynamics of the CoM resemble to a oscillatory behavior of a mass-spring system. That may be true during steady human gait but as soon as the movements are different (i.e. jumping, turning, running, ...), this assumption may not be true anymore and will lead to bad predictions of the GRFs.

2.3 Model 3: Krüger et al.

This third model^[4] is much more complex than the models presented in previous sections. Indeed, this model consist mainly in an optimization problem. It has been developed by Daniel Krüger and Sandro Wartzack (2017), they also developped a plugin for OpenSim (Delp et al. 2007) where they added the possibility to add point-on-plane contact element to OpenSim's modeling library and provided also an analysis algorithm that solves the force optimization problem by applying an interior point method (Wächter and Biegler 2006)¹.

2.3.1 Contact model

Like all surface forces, a contact force can be decomposed into three orthogonal components:

$$\begin{aligned}\mathbf{F}_n &= -\lambda_n \cdot \mathbf{n} \cdot \omega(d) \\ \mathbf{F}_{s1} &= \lambda_{s1} \cdot \mathbf{e}_1 \cdot \omega(d) \\ \mathbf{F}_{s2} &= -\lambda_{s2} \cdot \mathbf{e}_2 \cdot \omega(d)\end{aligned}\tag{6}$$

where \mathbf{F}_n is the normal component (directed in the negative direction of the plane's normal vector \mathbf{n}), \mathbf{F}_{s1} and \mathbf{F}_{s2} the two shear components that arise due to friction and inhibit a relative motion along the contact surface, $\omega(d)$ is a weighting function that scales the scale the entire contact force system dependant on the point-on-plane distance d . Normal force and shear forces are modeled according to the Coulomb's law for dry friction.

2.3.2 Optimization problem

We consider a schematic multibody system (Fig. 4), whose equations of motion take the general form:

$$\mathbf{M}(\mathbf{q})\ddot{\mathbf{q}} - \mathbf{Q}(\mathbf{q}, \dot{\mathbf{q}}) = \mathbf{F}_p(t, \mathbf{q}, \dot{\mathbf{q}}) + \mathbf{F}_c(\mathbf{q}, \dot{\mathbf{q}}, \boldsymbol{\alpha}, \boldsymbol{\lambda})\tag{7}$$

where \mathbf{M} is the mass matrix which captures the inertia properties, \mathbf{Q} is a vector containing the velocity dependent gyroscopic and Coriolis forces, \mathbf{F}_p is a vector of prescribed forces (i.e. gravity, springs, dampers, ...), \mathbf{F}_c is a vector of controllable forces which depends of unknown parameters).

All quantities are expressed in the space of the generalized coordinates \mathbf{q} . For inverse dynamic analysis of the multibody system we presume that its kinematic trajectory is

¹Source code available on <https://simtk.org/projects/statopt-contact>.

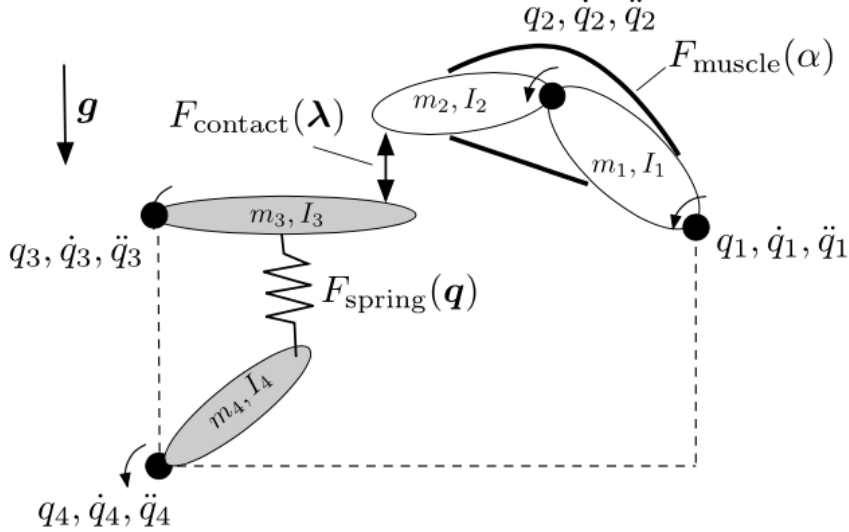


Figure 4: Schematic multibody system with prescribed and controllable forces.

known and documented as a time series of generalized coordinates $\hat{\mathbf{q}}(t)$. An approximation of this position trajectory by a twice differentiable spline function delivers the velocities $\dot{\hat{\mathbf{q}}}(t)$ and the accelerations $\ddot{\hat{\mathbf{q}}}(t)$. At every instance in time the unknown muscle activities $\boldsymbol{\alpha}(t)$ and contact multipliers $\boldsymbol{\sigma}(t)$ are obtained as a solution of the following constrained optimization problem:

$$\min_{\boldsymbol{\alpha}, \boldsymbol{\lambda}} \quad f(\boldsymbol{\alpha}, \boldsymbol{\lambda}), \quad (8a)$$

$$\text{subject to} \quad \alpha_{min} \leq \alpha \leq \alpha_{max}, \quad (8b)$$

$$\lambda_{min} \leq \lambda \leq \lambda_{max}, \quad (8c)$$

$$h_i(\boldsymbol{\alpha}, \boldsymbol{\lambda}) = 0, \quad (8d)$$

$$g_i(\boldsymbol{\lambda}) \geq 0. \quad (8e)$$

where the objective function (eq. 8a) is given as follows:

$$f(\boldsymbol{\alpha}, \boldsymbol{\lambda}) = \boldsymbol{\alpha}^T \boldsymbol{\alpha} + \frac{1}{w_0} \cdot \boldsymbol{\lambda}^T \boldsymbol{\lambda} \quad (9)$$

Where the activity of the muscles is defined by the active fiber force normalized by the maximum force the fibers can generate at their current length and contraction velocity:

$$\alpha_i = \frac{F_i}{F_{i,max}(q, \dot{q})} \quad (10)$$

Therefore, the first term of our objective function (eq. 9) fosters the recruitment of stronger muscles to relieve the weaker.

The second term in the objective function (eq. 9) minimizes the squared sum of contact multipliers and allows us to gradually deactivate contacts that are geometrically not

engaged. The weighting function, which we refer in equation 6, is defined as following and is graphically represented in Figure 5:

$$w(d) = \frac{1}{2} \cdot \left[1 + \tanh \left(-\pi \cdot \frac{2(d - d_{tol}) - d_{trans}}{d_{trans}} \right) \right] \quad (11)$$

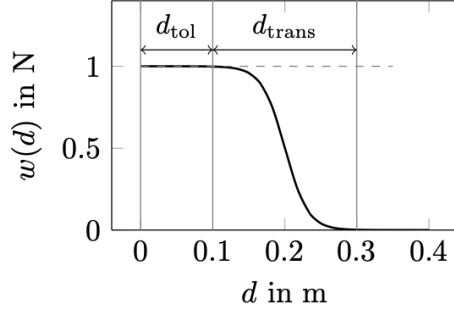


Figure 5: Weighting function assigned to a contact force system. With increasing distance between the contacting geometries the contact becomes gradually weaker until it is completely deactivated.

2.4 Model 4: *Geijtenbeek et al.*

This model^[6] has been developed by T. Geijtenbeek, A. J. van den Bogert, B. J. H. van Basten and A. Egges (2010). It aims to have a realistic model of movement to animate a virtual character. In this section we will therefore describe in detail how a musculoskeletal model can be used to evaluate the ground reaction forces applied during a movement.

2.4.1 Musculoskeletal model

As for the previous method, the model incorporates both the skeletal and muscular structure of the entire human body and can be described using a tuple \mathcal{H} :

$$\mathcal{H} = \{\mathcal{B}, \mathcal{Q}, \mathcal{U}\} \quad (12)$$

where the set \mathcal{B} describes the individual body segments which have specific mass, inertial properties and reference position and orientation, the set \mathcal{Q} describes the n kinematic-degrees of freedom of the model and the set \mathcal{U} describes the l muscles in the model.

As this paper aim to animate virtual characters, the input for the method is an animation \mathbf{A} , consisting of a sequences of T frames:

$$\mathbf{A} = \{A_1, A_2, \dots, A_T\} \quad , \quad A_t = \{q_t, \dot{q}_t, \ddot{q}_t, S_t^l, S_t^r\} \quad (13)$$

where q_t is a pose vector representing the n kinematics degrees of freedom defined in \mathcal{Q} , \dot{q}_t and \ddot{q}_t are first and second order derivatives of q_t . S_t^l and S_t^r are polygons representing the ground contact region at frame t , for left and right foot respectively.

2.4.2 Method of prediction

Calculate external force and moment The external force and moment F_e and M_e that acts on the character at frame A_t . This is done by resolving the dynamics equation of the motion defined by q_t , \dot{q}_t and \ddot{q}_t , which can be formulated as:

$$\mathbf{M}(q_t)\ddot{q}_t + \mathbf{T}(q_t)\tau + c(q_t, \dot{q}_t) = 0 \quad (14)$$

where $\mathbf{M}(q_t)$ is an $n \times n$ matrix that describes the pose dependent mass distribution based on \mathcal{B} and \mathcal{Q} , the vector τ contains the (unknown) moments and forces, the vector $c(q_t, \dot{q}_t)$ are gravitational, centrifugal and Coriolis forces, $\mathbf{T}(q_t)$ is an $n \times n$ coefficient matrix that has no specific meaning. From re-arranging the equation 14 we get:

$$\tau = \mathbf{T}(q)^{-1} [\mathbf{M}(q)\ddot{q} + c(q, \dot{q})] \quad (15)$$

Then the external force and moment F_r and M_r acting on the root element of the character must be expressed in the global coordinate frame, F_e and M_e that is defined as:

$$F_e = \mathbf{R}^{-1}F_r \quad , \quad M_e = \mathbf{R}^{-1}M_r + r \times (\mathbf{R}^{-1}F_r) \quad (16)$$

where \mathbf{R} is the orientation matrix and r is the origin

Estimate Ground Reaction Forces Then, we need to estimate the ground reaction forces and moment for both foot. The ground reactions forces are bound by the following constrains:

1. At least one foot must be in contact with the ground before there can be any ground reaction forces ($S_t^l \cup S_t^r \neq \emptyset$).
2. The external force F_e must point upwards, otherwise it cannot be attributed to ground contact ($F_{e,y} > 0$).
3. The horizontal component of the ground reaction force must be in agreement with the Coulomb friction model ($\|F_{e,xz}\| \leq \|F_{g,y}\|$).
4. The origin of the ground reaction force and moment for each foot must lie within the support polygon of the corresponding foot.

No dynamic friction model has been used in this model.

The ground reaction force and moment applied to each foot must originate from a point on $y = 0$ that lies within the respective support polygon. This imposes a constraint on the ground reaction moment around x and z . To apply this constraint, we first define c_e as the point on $y = 0$ from which F_e and M_e would originate:

$$c_{e,x} = \frac{M_{e,z}}{F_{g,y}} \quad , \quad c_{e,z} = \frac{-M_{e,xz}}{F_{g,y}} \quad (17)$$

If c_e lies outside a support polygon S , we define the origin, c_g , as the point inside S that is closest to c_e .

The reaction $M_{g,x}$ and $M_{g,z}$ moments then become:

$$M_{g,x} = -c_{g,z}F_{g,y} \quad , \quad M_{g,z} = c_{g,x}F_{g,y} \quad (18)$$

In cases where both feet are in contact with the ground, the computation of (18) is performed individually for each foot. The force and moments are then weighted according to the distance between c_e and support polygons S_t^l and S_t^r and are defined as:

$$\omega_l = \frac{d(c_e, S_t^l)}{d(c_e, S_t^l) + d(c_e, S_t^r)} \quad , \quad \omega_r = \frac{d(c_e, S_t^r)}{d(c_e, S_t^l) + d(c_e, S_t^r)} \quad (19)$$

where ω_l is the scaling factor applied to acquire F_g^l and M_g^l , and ω_r is the scaling factor applied to acquire F_g^r and M_g^r .

2.5 Model 5: *Karatsidis*

The last approach [7] has been developed by Angelo Karatsidis during his doctoral thesis presented in 2018. It consists in many chapter but we will only be interested in the 2nd chapter: *Estimation of Ground Reaction Forces and Moments During Gait Using Only Inertial Motion Capture*.

The Experimental protocol used in this thesis is mostly similar to the approach used in 2.1. Therefore, from the data acquired using multiple markers and IMUs mounted on a suit which the model was wearing. The markers were detected using the optical motion capture (OMC) system. From those data, the inverse kinematics allows to reconstruct the model's pose at each moment of the experiment. Then, they assumed that the GRF&Ms are the only significant external loads present. Thus, the total external force and moment can be derived from Newton and Euler equations of motion, respectively (eq. 20 and 21).

$$\mathbf{F}_L + \mathbf{F}_R = \mathbf{F}_{ext} \quad (20)$$

$$\mathbf{M}_L + \mathbf{M}_R = \mathbf{M}_{ext} \quad (21)$$

where \mathbf{F}_L , \mathbf{F}_R and \mathbf{M}_L , \mathbf{M}_R are the ground reaction forces and moments applied on the left and right foot, respectively.

During the single support phase, the result of the computation is the GRF&M applied on the foot, which is in contact with the ground. The resulting GRM is expressed about the external contact point on that foot, which is chosen as the projection of the ankle joint on the ground. During double support phase, they applied a distribution algorithm based on a smooth transition assumption function (f_{STA}), which was constructed from empirical data similarly to previous studies ([8]). Subsequently, a cubic spline interpolation function was used to generate the f_{STA} . The different cubic spline interpolation for each component of the GRF&M are represented in the Figure 6. To distinguish between the phases of single and double stance, they used a gait event detection algorithm based on a threshold in the norm of the velocities of the heel ($\|v_{heel}\|$)

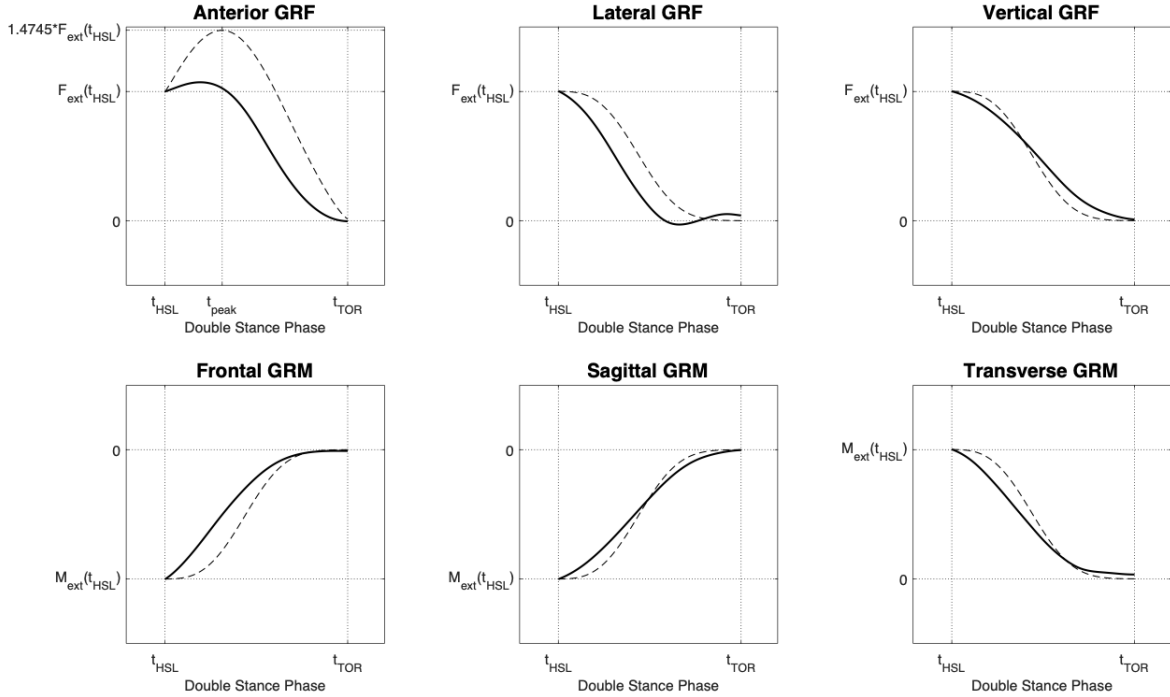


Figure 6: The curves of the smooth transition assumption function for the three GRF components ($f_{F,STA}$, three graphs on the top) and three GRM components ($f_{M,STA}$, three graphs on the bottom) used to distribute the total external force and moment among the two feet. Figure illustrates the curve of the GRF&Ms of the right foot between the events of left heel strike and right toe off (second double stance phase) expressed in the coordinate system defined by the walking direction. Continuous lines indicate the curves obtained from the average values across all subjects and trials of our dataset, whereas dashed lines indicate the curves proposed by Ren et al.^[8].

and the toe ($\|v_{toe}\|$). From these values, a final state machine (FSM) is implemented to detect the current state of the gait cycle, as represented in Figure 7.

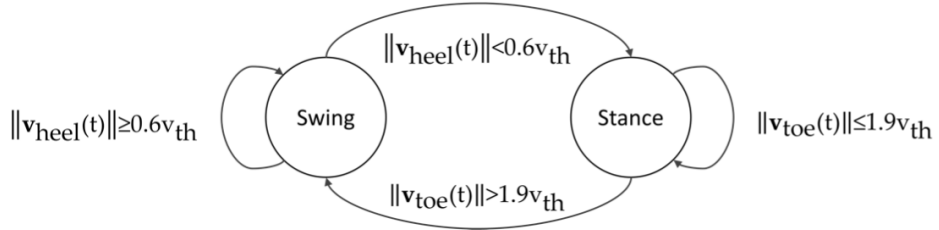


Figure 7: A state machine to detect the current state of the gait cycle, based on the previous state and a condition on the velocity of the heel or toe. The velocity $\|v_{th}\|$ is equal to the norm of the average velocity of the pelvis segment for each trial.

3 Implemented models

During the project, a total of three approaches have been implemented. Firstly, the general protocol and the processing of the data will be developed as they are identical for all implemented models. Then a general description of the model operation will be developed.

Henceforth, all points are expressed in the global ground frame (illustrated in Figure 8). The x-axis direction corresponds to the walking direction. The y-axis points upwards and the z-axis points on the right-hand side of the body. In the global ground frame, the body frame has no speed in the x-axis. It facilitates the gait analysis as there are no dependencies of the body speed and direction.

3.1 Experimental protocol

As for most of the previous approaches, the simulated body model incorporates both the skeletal and the muscular structure of the lower part of the human body. Then, for the simulated model to move the same way the actual subject is moving, 39 reflective markers were placed on the subject. An OMC system, including infrared high-speed cameras (frequency= 60Hz), was used to capture the reflective markers mounted on the body and their position.

Then the model was scaled in order to have similar size and weight distribution between the simulated body's elements and the actual subject's members ([9], [10], [11] and [12]).

To assess the quality of the obtained results during the simulation, there are experimental data that were obtained using force plates. It is a measurement devices embedded in the floor of a laboratory. These data are composed, for each

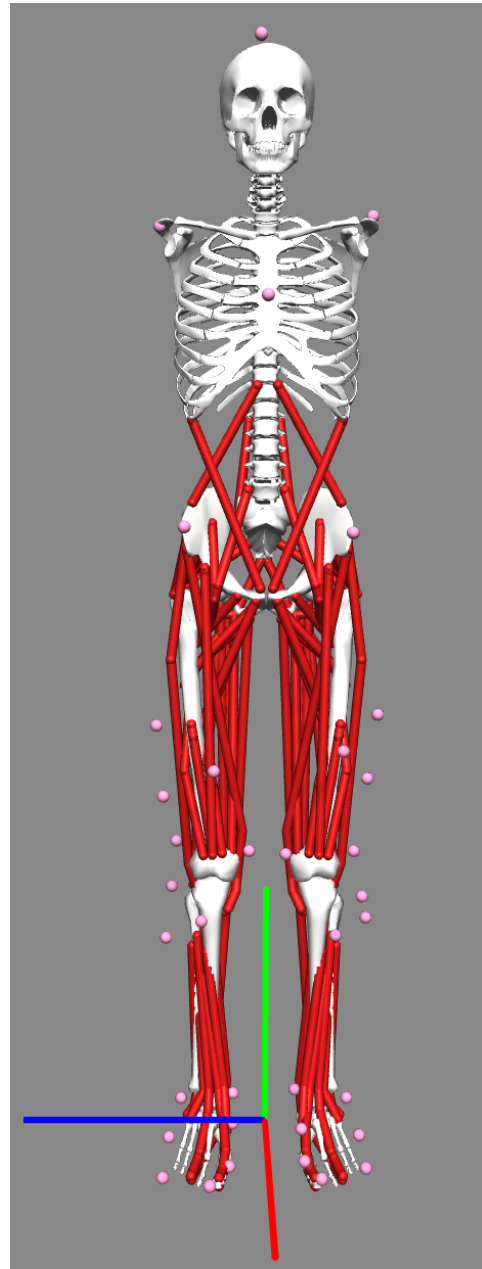


Figure 8: Representation of the skeletal and the muscular structure of the model on Opensim Software. The pink dots represent the markers' position on the model. The global frame axis are also represented: X-red, Y-Green, Z-Blue

sampling time (frequency= $600Hz$), of the Force Application Point (FAP) of the ground reaction force for each foot, their magnitude and the ground reaction moment for each foot.

Thus, the section 4 which presents the results is using these data as groundtruth data (the experimental data have been down-sampled by a factor 10 to allow the comparison).

3.2 Data processing

From this model and the experimental markers' position, the inverse kinematics was performed. The inverse kinematics² is the process during which experimental markers are matched by model markers throughout the motion by varying the joint angles (generalized coordinates) through time. Once the inverse kinematics has been processed and the model is thus moving similarly to the actual subject, a second process is applied to the model, called inverse dynamics³. It allows to determine the generalized forces (e.g., net forces and torques) at each joint responsible for a given movement. Given the kinematics (e.g., motion) describing the movement of a model and a portion of the kinetics (e.g., external loads) applied to the model, we then obtain the residual moment and force (expressed in local frame of pelvis) applying on the pelvis (e.g., mostly the external forces).

To obtain the residual moment and force, the software Opensim make the usage of the Residual Reduction Algorithm (RRA)⁴. Finally, the residual force and moment must be transformed from the pelvis frame to the ground frame. This is done in the same way as the inverse kinematics and dynamics, using opensim's APIs⁵.

3.3 Data analysis

3.3.1 Implemented model 1

The first model consists in implementing the model presented in section 2.4. The method used to estimate the external forces and moments is the one described in section 3.2 and it differs from the original method. Using the calculated external forces, the estimation of the GRF&M is done according to the original method.

As illustrated in Figure 9 (complementary results can be found in the Appendix B, Figures 22, 23, 24, 25 and 26), the shape of the predicted and experimental forces are similar but it is not exactly following the experimental data. Moreover, during the transition phase (e.g., the double stance phase), the forces does not have a smooth evolution, which is not representative of the reality. This can be explained by the poor

²Opensim documentation - Inverse kinematics <https://simtk-confluence.stanford.edu:8443/display/OpenSim/Getting+Started+with+Inverse+Kinematics>

³Opensim documentation - Inverse dynamics <https://simtk-confluence.stanford.edu:8443/display/OpenSim/Getting+Started+with+Inverse+Dynamics>

⁴Opensim documentation - Residual Reduction Algorithm <https://simtk-confluence.stanford.edu:8443/display/OpenSim/How+RRA+Works>

⁵Opensim documentation - Frame class https://simtk.org/api_docs/opensim/api_docs/classOpenSim_1_1Frame.html

estimation of the CoP (as showed in eq. 17, the computation of the CoP is related to the estimated moment).

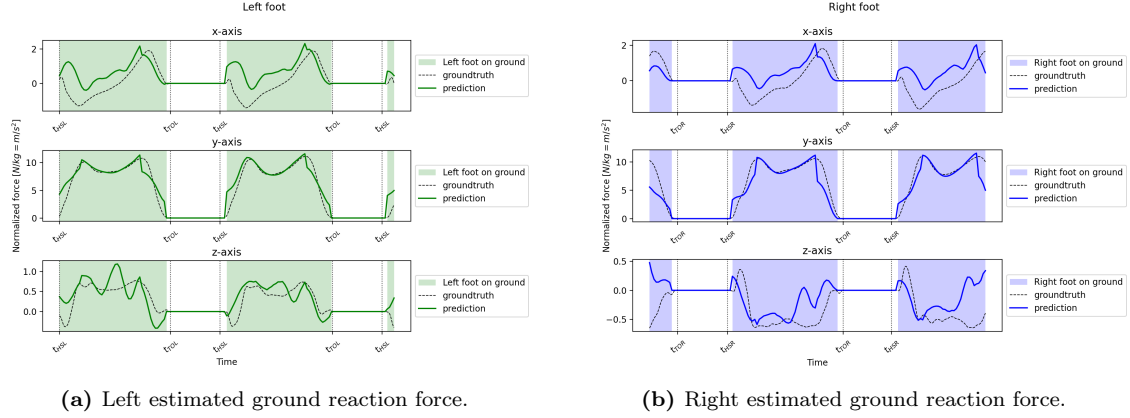


Figure 9: Graphical representation of the predicted and experimental GRF for the first implemented model. Curve magnitudes are normalized to body weight, thus, the units are in $N/kg = m/s^2$. t_{HSX} stands for the time at which the left or right heel strikes the ground (with $X = L$ or R , respectively) and t_{TOX} the time at which the left or right toes are lifting off from the ground (with $X = L$ or R , respectively)

3.3.2 Implemented model 2

The second model consists in implementing an adapted model from the one presented in section 2.1. Firstly, the method used to estimate the external forces and moments is the one described in section 3.2. Then, using the same point distribution as illustrated in Figure 12 and by considering each point as an actuator that can apply a force. The computed total force is distributed between the points proportionally to their height from the ground if they are close enough to the ground. However, in order to prevent discontinuities in the predicted GRF&Ms due to the sudden transition of a point from inactive to fully active a smoothing function has been defined in equation 22 and illustrated in Figure 10.

$$u_{smooth} = 0.5 \left(\tanh \left(-\pi \cdot \frac{2(u_{ratio} - u_{th}) - (1 - u_{th})}{1 - u_{th}} \right) + 1 \right) \quad (22)$$

where u_{smooth} represents the smoothed value given an input u_{ratio} and u_{ratio} being the ratio between the actual height or speed and a threshold value.

As illustrated in Figure 11, the correspondence criteria between the experimental data and predicted GRF&Ms aren't really met. Moreover, the different phases are not very well detected. This model could be improved, but due to time consideration, the development of the last model has been favored despite the development of this model because it was less promising. However it has some advantages that will be discussed in section 5.

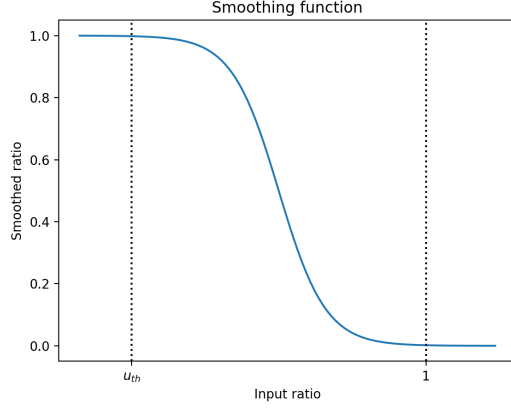


Figure 10: Smoothing function used to avoid sudden transition.

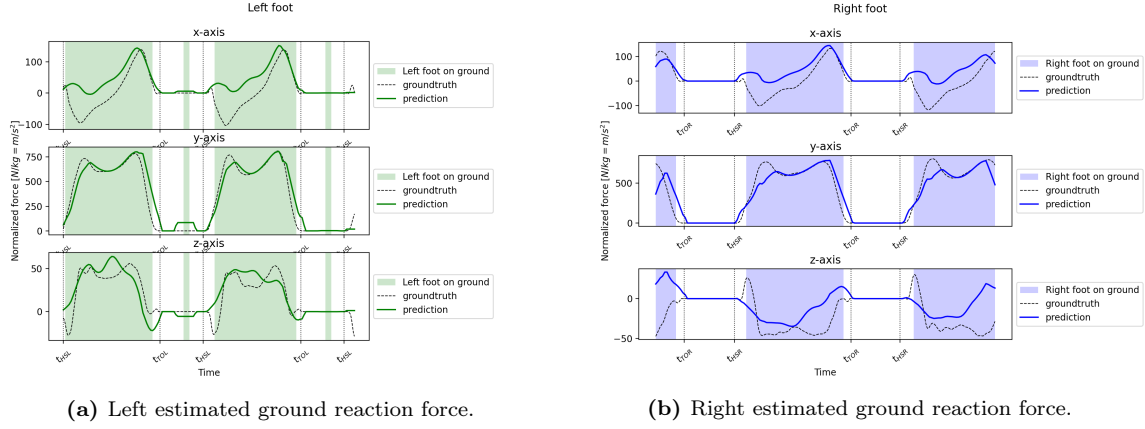


Figure 11: Graphical representation of the predicted and experimental GRF for the first implemented model. Curve magnitudes are normalized to body weight, thus, the units are in $N/kg = m/s^2$. t_{HSX} stands for the time at which the left or right heel strikes the ground (with $X = L$ or R , respectively) and t_{TOX} the time at which the left or right toes are lifting off from the ground (with $X = L$ or R , respectively)

3.3.3 Final implementation

The final model implementation takes some inspiration in previous models and mostly the ones presented in sections 2.1 and 2.5.

FAP estimation The computation of the FAP (Force Application Point) is usually computed using dynamics data by considering the estimated force and moment (see eq. 17 for more details). As the moment estimation is not very precise, it was not possible to estimate the position of the CoP (Center of Pressure) with a good accuracy. Thus, instead of estimate the CoP, we estimate the FAP for each foot using only kinematics data (positional data).

To determine the position of the FAP on one foot, N points ($N = 11$ in our case) are set on the foot sole. The position of these points are represented on Figure 12.

At each time step, their position can be retrieved from the model pose. By taking

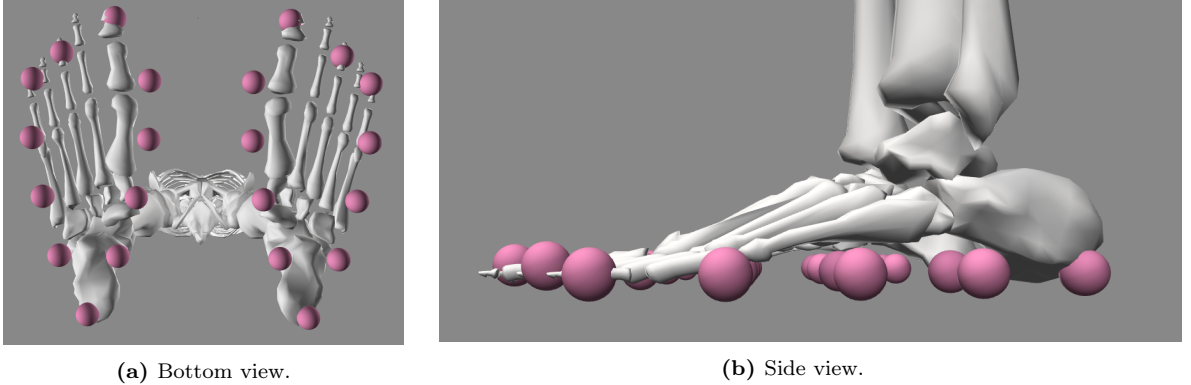


Figure 12: Representation of the points' position used to estimate the FAP (Force Application Point) for each foot.

their distance to the ground (e.g., y-component in ground frame), one can estimate the position of the FAP. First, the weight of each point is calculated using the softmax activation function defined in equation 23.

$$\mathbf{w}_i = \frac{e^{-\mathbf{p}_{i2}}}{\sum_{i=1}^N e^{-\mathbf{p}_{i2}}} \quad (23)$$

where \mathbf{w}_i represents the activation rate of the i^{th} point, \mathbf{p}_{i2} corresponds to the y-component of the position of the i^{th} point and N is the number of points.

Then, using the previously calculated weights, one compute the weighted average in each dimension using the following equation:

$$\mathbf{FAP}_i = \begin{cases} \frac{1}{N} \sum_{j=1}^N \mathbf{w}_j \mathbf{p}_{ji}, & \text{if } i = 1, 3 \\ 0, & \text{if } i = 2 \end{cases} \quad (24)$$

where \mathbf{FAP}_i represents the position of the FAP for the i-component (1-x, 2-y, 3-z), \mathbf{p}_{ji} corresponds to the i-component of the j^{th} point and N is the number of points.

The y-axis is set to zero, this is due to the fact that the FAP must lie on the ground.

Determination of the gait cycle's phases Similarly to the approach used in the method presented in 2.5, to distinguish between the phases of single and double stance, a gait event detection algorithm based on a threshold in the norm of the velocities of the heel ($\|v_{heel}\|$) and the toe ($\|v_{toe}\|$) is used. Thus, a final state machine (FSM) is implemented as represented in Figure 13.

The FSM allows to determine whether or not right and leg feet are in contact with the ground, these results are then used in the next step.

Interpolation of the force and moments using cubic splines Knowing the state of each foot at each moment, we can then estimate the GRF&M and its distribution

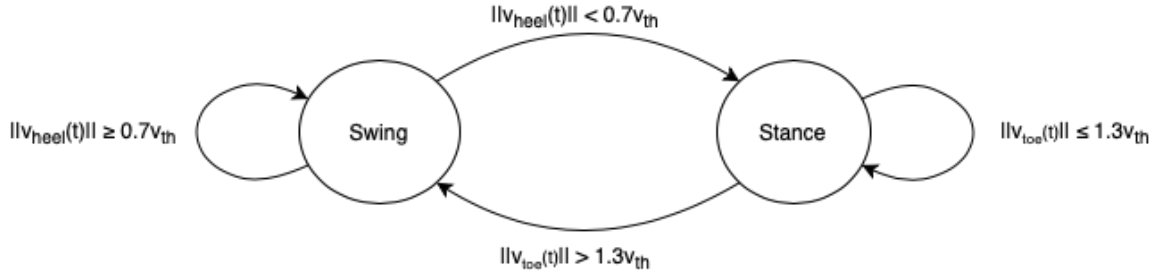


Figure 13: A final state machine to detect the current state of the gait cycle, based on the previous state and a condition on the velocity of the heel or toe. The velocity v_{th} is equal to the norm of the average velocity of the pelvis segment for each trial.

between the legs. During the single support phase, the result of the computation is the GRF&M applied on the foot which is in contact with the ground. However, during the phase of double support, the system of equations is indeterminate. To overcome this, cubic interpolation allows a smooth transition of the force distribution from one leg to the other. To illustrate that, Figure 14 shows the smooth transition of the force distribution between 2 states.

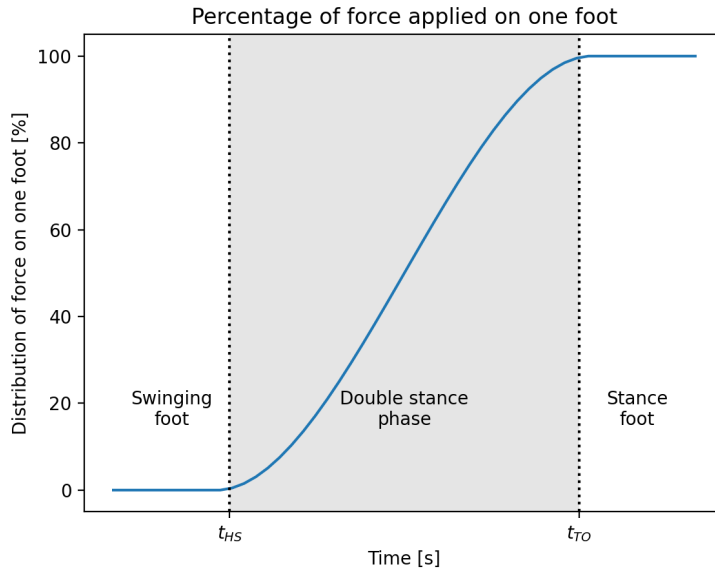


Figure 14: The curve shows the smooth transition of the force distribution on one foot while passing from the swinging state ($t < t_{HS}$, no GRF&M on the foot), to the double stance phase ($t_{HS} < t < t_{TO}$) and finally to the single stance phase ($t_{TO} < t$), where t_{HS} stands for the time at which the heel strikes the ground and t_{TO} the time at which the toes are lifting off from the ground.

Using the cubic splines⁶, it is possible to interpolate the distribution factors between the two feet at each time. As of now, factors are only known during the single support

⁶The cubic splines used in this method are much simpler than the one used in the approached presented in section 2.5 for simplicity reasons. These differences are discussed in section 5.

phases, the factor of the foot on the ground is equal to 1 while the other one is equal to 0. During the transition from one foot to the other (e.g., double support phase), the transition between the 2 values is done by interpolating the factors with a cubic splines (the resultant distribution of the factors during the experiment is depicted in the next section, see Fig. 17).

Finally, using the previous computed factors, one multiplies them with the calculated forces and moments which gives the forces and moments for both left and right feet.

In Table 1, the values of each variable are summed up for a better understanding of the distribution over time.

Variable	Left Stance Phase	Double Stance Phase	Right Stance Phase
$\mathbf{F}_R(t)$	0	$\mathbf{F}_{ext}(t) \cdot f_R(t)$	$\mathbf{F}_{ext}(t)$
$\mathbf{F}_L(t)$	$\mathbf{F}_{ext}(t)$	$\mathbf{F}_{ext}(t) \cdot f_L(t)$	0
$\mathbf{M}_R(t)$	0	$\mathbf{M}_{ext}(t) \cdot f_R(t)$	$\mathbf{M}_{ext}(t)$
$\mathbf{M}_L(t)$	$\mathbf{M}_{ext}(t)$	$\mathbf{M}_{ext}(t) \cdot f_L(t)$	0

Table 1: Summary of the value of each force and moments at each time. The functional $f_X(t)$ corresponds to the distribution factor of the left or right foot (with $X = L$ or R , respectively). Moreover, one can admit that $f_R(t) = 1 - f_L(t)$ at all time.

4 Results

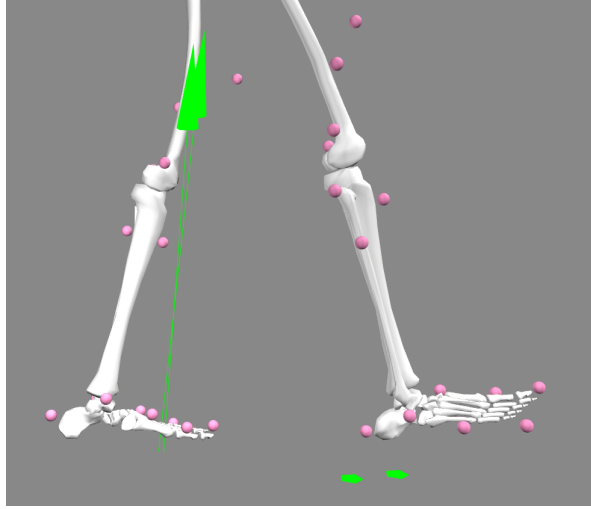


Figure 15: Illustration of the predicted force and experimental force visualized on Opensim software.

To evaluate the accuracy of the method, the root mean square errors (RMSE) and the relative root mean square errors (rRMSE) are used. The RMSE and rRMSE used in this section are defined in equations 25 and 26, respectively.

$$RMSE = \sqrt{\frac{1}{N} \sum_{i=0}^N (u_{pred,i} - u_{exp,i})^2} \quad (25)$$

$$rRMSE = \frac{RMSE}{\max_{0 \leq i < N} u_{exp,i} - \min_{0 \leq i < N} u_{exp,i}} \quad (26)$$

with u_{exp} being the experimental force or moment, u_{pred} the predicted force or moment and N the number of samples.

Another metric is also used to assess the correlation between the predicted GRF&M and the experimental data, the Pearson product-moment correlation coefficient (ρ) that measures linear correlation between two variables. It has a value between 1 and -1, where 1 is total positive linear correlation. The resulted coefficients can be categorized in different categories: weak ($\rho \leq 0.35$), moderate ($0.35 < \rho \leq 0.67$), strong ($0.67 < \rho \leq 0.9$) and excellent ($0.9 < \rho$), according to Fluit et al.[13].

Finally, using the predicted GRF&M and the experimental GRF&M, we assess the feasibility of the dynamics.

FAP estimation The first step is to estimate where the force and moments are applied (e.g., the FAP). The method used is described in section 3.3.

After applying this method the obtained results, presented in Table 2 and in Figure 16 (shows the estimated FAP's position evolution over time), are very close to the experimental data. Indeed, the correlation coefficient between them for the x-axis is

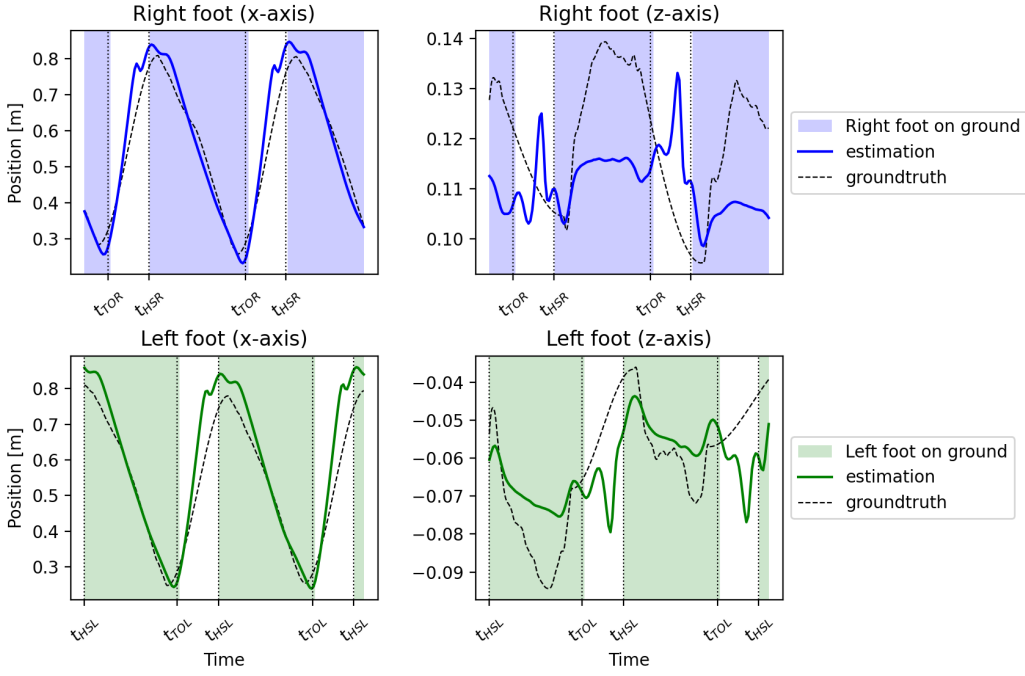


Figure 16: Evolution of the estimated and experimental FAP’s position over time for xz-axis and both feet. Y-axis is not represented as the value is constant and is situated at the border between the ground and the foot.

t_{HSx} stands for the time at which the left or right heel strikes the ground (with $x = L$ or R , respectively) and t_{TOx} the time at which the left or right toes are lifting off from the ground (with $x = L$ or R , respectively).

equal to 0.98 and the RMSE is equal to 0.5cm in average. As defined previously, a correlation of 0.98 is considered as excellent. Thus the x-component of the FAP is very well estimated. The y-axis is not taken into account because the point is situated at the border between the foot and the ground which is a constant value. Concerning the z-axis, the results are not as good, this is mainly due to the fact that the variance is much smaller on this axis and, thus, it is more subject to the noise in the measurements. Indeed, as we can see on Figure 16, experimental data are not periodic over a gait cycle for the z-axis. To nuance that, the width of a foot is in order of 10cm, therefore a RMSE of 0.13cm (for the right foot) is still smaller from a factor 100 than the foot-width.

GRF&M estimation Once the two FAPs are found (e.g., point from which the forces originate), the GRF&M must be distributed between those 2 points. As explained in section 3.3, the gait cycles phases must be determined. From that, it is possible to distribute the estimated GRF&M using cubic splines.

The Figure 17 depicts the resultant distribution factors between the two legs. The sum of the factor is equal to 1 as all of the external load and moment are considered as GRF&M.

As explained before (sec. 3.3), the distribution factors are multiplied with the

foot, axis	RMSE [cm]	rRMSE [%]	ρ [a.u.]
right, x	0.42	0.76	0.98
right, y	0.00	0.00	1.00
right, z	0.13	2.89	0.18
left, x	0.57	1.01	0.98
left, y	0.00	0.00	1.00
left, z	0.10	1.65	0.66

Table 2: Evaluation of the error between the experimental and the predicted data concerning the FAP using RMSE, rRMSE and ρ (e.g., Pearson product-moment correlation) during the whole experiment (duration of 2.5s). The analysis has been done separately for each foot and for the each dimension.

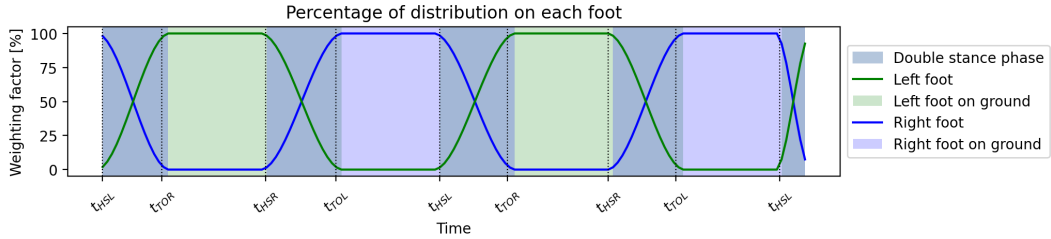


Figure 17: Distribution between each foot. The sum of the right weight and the left is always equal to 100% considering that they are the only element in contact with the ground.

t_{HSX} stands for the time at which the left or right heel strikes the ground (with $X = L$ or R , respectively) and t_{TOX} the time at which the left or right toes are lifting off from the ground (with $X = L$ or R , respectively).

external forces to get the resultant forces on both left and right feet.

The obtained graphical results are shown on Figures 18 and 19 for the left and right foot, respectively. Statistical analysis results are presented in Table 3. As before, we obtain relatively small RMSE and rRMSE (4.49N and 1.59% in average, respectively). Similarly to the FAP estimation, the main component (e.g., the x-axis for FAP and y-axis for the GRF) is very well estimated. Indeed, the correlation coefficient is equal to 0.96 for both feet which is considered as excellent correlation. The correlation for the other component can only be classified as moderate to strong ($\rho = 0.39$ to 0.77)

foot, axis	RMSE [N]	rRMSE [%]	ρ [a.u.]
right, x	4.21	1.69	0.64
right, y	7.86	0.98	0.95
right, z	2.04	2.63	0.39
left, x	4.21	1.74	0.66
left, y	7.25	0.89	0.96
left, z	1.37	1.61	0.77

Table 3: Evaluation of the error between the experimental and the predicted data concerning the GRF using RMSE, rRMSE and ρ (e.g., Pearson product-moment correlation) during the whole experiment (duration of 2.5s). The analysis has been done separately for each foot and for the each dimension.

The GRM is obtained similarly to the way the force is obtained.

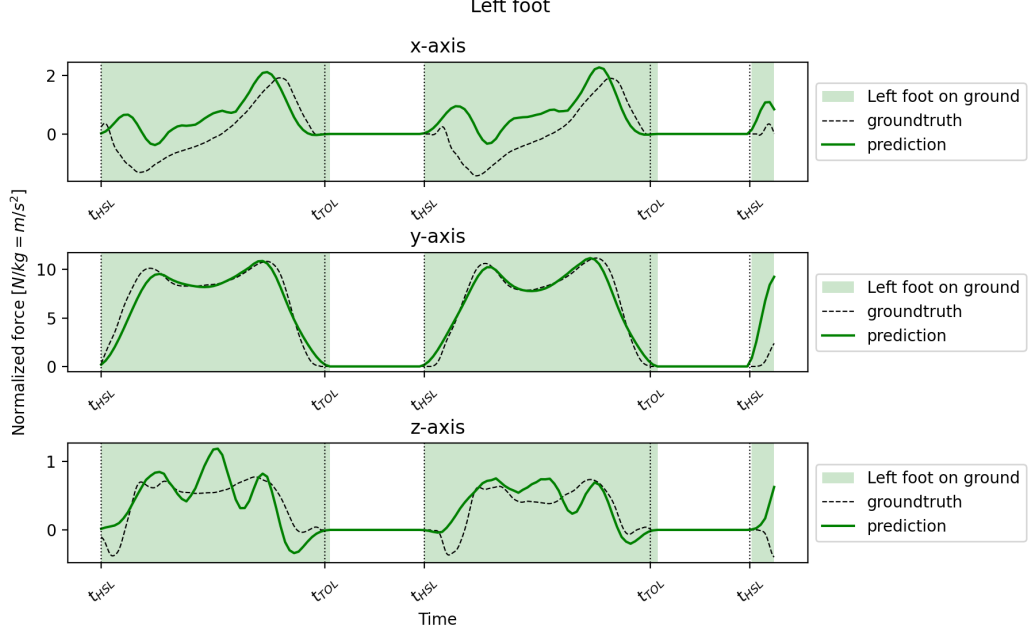


Figure 18: Graphical representation of the predicted and experimental GRF. Curve magnitudes are normalized to body weight, thus, the units are in $N/kg = m/s^2$.

t_{HSX} stands for the time at which the left or right heel strikes the ground (with $X = L$ or R , respectively) and t_{TOX} the time at which the left or right toes are lifting off from the ground (with $X = L$ or R , respectively).

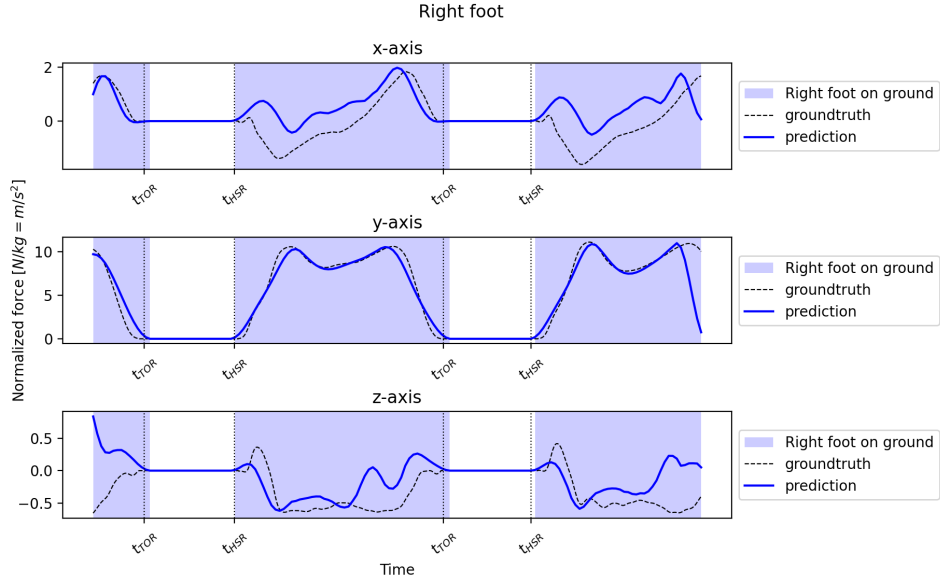


Figure 19: Graphical representation of the predicted and experimental GRF. Curve magnitudes are normalized to body weight, thus, the units are in $N/kg = m/s^2$.

t_{HSX} stands for the time at which the left or right heel strikes the ground (with $X = L$ or R , respectively) and t_{TOX} the time at which the left or right toes are lifting off from the ground (with $X = L$ or R , respectively).

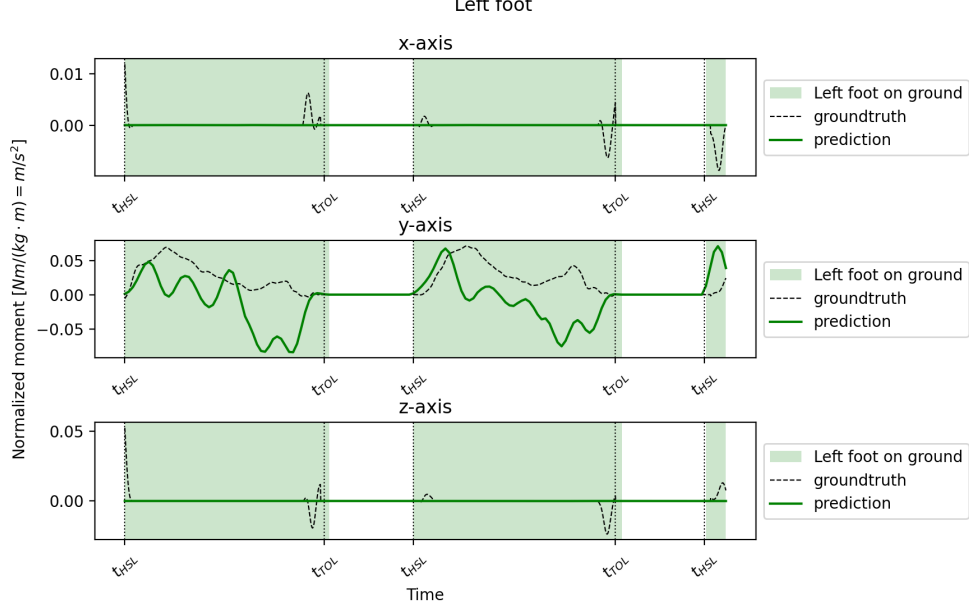


Figure 20: Graphical representation of the predicted and experimental GRM. Curve magnitudes are normalized to body weight times body height, thus, the units are in $Nm/(kg \cdot m) = m/s^2$.

t_{HSX} stands for the time at which the left or right heel strikes the ground (with $X = L$ or R , respectively) and t_{TOX} the time at which the left or right toes are lifting off from the ground (with $X = L$ or R , respectively).

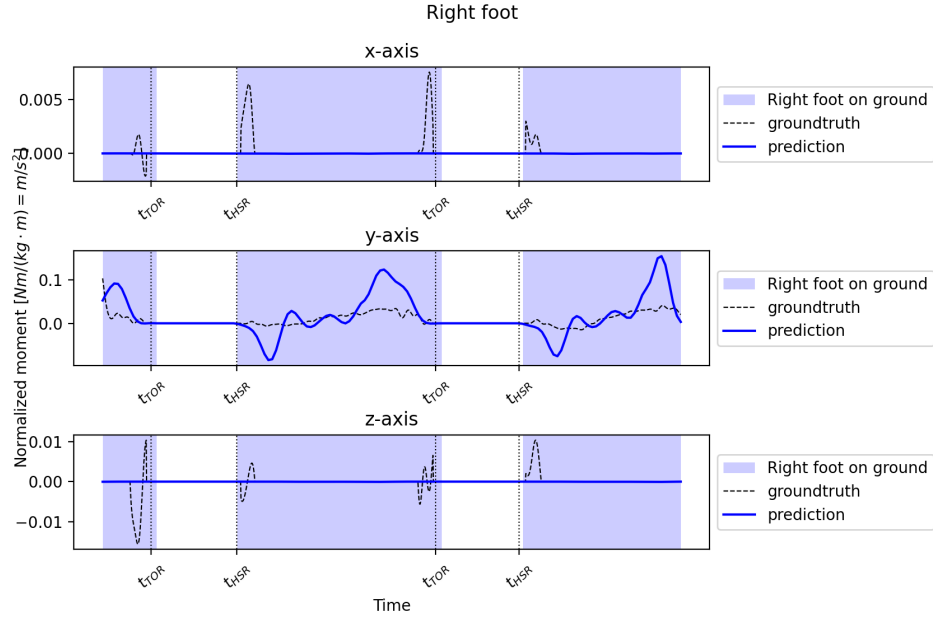


Figure 21: Graphical representation of the predicted and experimental GRM. Curve magnitudes are normalized to body weight times body height, thus, the units are in $Nm/(kg \cdot m) = m/s^2$.

t_{HSX} stands for the time at which the left or right heel strikes the ground (with $X = L$ or R , respectively) and t_{TOX} the time at which the left or right toes are lifting off from the ground (with $X = L$ or R , respectively).

The obtained graphical results are shown on Figures 20 and 21 for the left and right foot, respectively. Statistical analysis results are presented in Table 3. The results show a weak correlation ($\rho < 0.14$) except for the right foot in the y-axis where it is strongly correlated ($\rho = 0.72$).

foot, axis	RMSE [Nm]	rRMSE [%]	ρ [a.u.]
right, x	0.01	0.89	0.14
right, y	0.38	2.44	0.72
right, z	0.02	0.68	-0.02
left, x	0.02	0.60	0.04
left, y	0.46	4.54	-0.12
left, z	0.06	0.57	-0.05

Table 4: Evaluation of the error between the experimental and the predicted data concerning the GRM using RMSE, rRMSE and ρ (e.g., Pearson product-moment correlation) during the whole experiment (duration of 2.5s). The analysis has been done separately for each foot and each dimension.

Inverse dynamics with external forces As a final step, one compute the inverse dynamics using known external forces (e.g. predicted GRF&M and experimental GRF&M). In table 5, we can see that the errors between the found moments for both experimental and predicted GRF&Ms. As we can see the differences can be important for some joints ($rRMSE_{pelvis_tilt_moment} = 118.80\%$, illustrate in Figure ??), but in general the shape (see Figures 27, 28 and 29 in Appendix B) is similar, the experimental moments are sometimes bigger than the expected moments.

Joints	RMSE [Nm]	rRMSE [%]
pelvis_tilt_moment	89.39	118.80
pelvis_list_moment	30.94	55.30
pelvis_rotation_moment	11.17	57.69
pelvis_tx_force	61.82	39.25
pelvis_ty_force	32.94	15.56
pelvis_tz_force	34.78	33.29
hip flexion_r_moment	56.87	55.02
hip adduction_r_moment	20.34	26.08
hip rotation_r_moment	6.07	36.33
hip flexion_l_moment	71.18	70.88
hip adduction_l_moment	16.06	17.96
hip rotation_l_moment	5.71	29.87
lumbar_extension_moment	0.71	2.61
lumbar_bending_moment	0.82	1.30
lumbar_rotation_moment	0.28	2.80
knee_angle_r_moment	36.67	36.98
knee_angle_l_moment	46.81	44.55
ankle_angle_r_moment	22.37	15.76
ankle_angle_l_moment	24.55	18.29

Table 5: RMSE and rRMSE between inverse dynamics using predicted and experimental GRF&Ms.

5 Discussion

As evoked before (sec. 3.2), external forces and moments are estimated using the Residual Reduction Algorithm. This method allows to get a relatively good estimation of the external forces. However it is not as precise to estimate the external moments. Indeed, Figures 22 and 23 (See Appendix B) illustrate well this assertion. On Figure 22, we can see that the general shape of the measured forces are well followed by Opensim’s estimation of the external force. In contrast to the Figure 23, we can see that the general shape of the measured moments are not as well followed by Opensim’s estimation of the external moments. This is a drawback that is difficult to compensate using Opensim’s method. It mainly explains the poor performance of the method that use the moments to estimates other variables (e.g. the center of pressure in the model described in section 3.3.1).

To overcome this limitation, in the final chosen implementation it is not the center of pressure (CoP) which is estimated, as it depends of the moment. Instead, for each foot, the Force Application Point (FAP) is estimated using only kinematics data (i.e. position of points distributed on the foot sole). As the experimental data are composed of the FAP and their magnitude, it also facilitates the comparison of the estimated data and the experimental data. Likewise to the final model, the second implemented model is not dependent to the moment apart from the estimation of the moment itself.

Even if the cubic splines are also used in the approach from Karatsidis (description of the model in sec. 2.5), the implementation are not similar. Indeed, as mentioned in the

description of the final model (sec. 3.3.3), the final implementation makes use of a single basic spline while in Karatsidis paper, the cubic splines are found experimentally from average values across all subjects and trials of their dataset. They also find different splines for each component of the forces and moments which gives a total of 6 different splines. The results were satisfying using a simple cubic spline, therefore there were no need to define more complex and different cubic splines for each component of the force and the moment.

The main drawback of the actual implementation is that it is not a real-time analysis. Indeed, the interpolation of the distribution factor between the two feet is done a posteriori. The two other implementations are working in real time which makes them also very interesting. In order to make the actual implementation working in real time it could be possible using more experimental data. By estimating the average time spent in the double stance phase, it could be possible to estimate the current distribution factor in a real time manner and thus, the final implemented could become a real time method.

As seen in the previous section, the inverse dynamics can be computed by considering the external forces (e.g. the GRF&Ms). After computing them, we observe similar shaped results while the required moments to observe these movements are sometimes bigger than expected. These differences could be explained by the bad estimation of the moments. Improving the ground reaction moment estimations could lead to a better inverse dynamics.

Finally, in order to improve the results, it could be possible to have more subjects and trials to have more precise statistical results. The different trials could also be in different activity. Indeed, it could be interesting to assess the the model in different condition than normal gait, such as running, jumping,

Appendices

A Abbreviations

- AMS:** AnyBody Modeling System
GRF&M: Ground Reaction Force and Moment
CoM: Center of Mass
CoP: Center of Pressure
FAP: CForce Application Point
OMC: Optical Motion Capture
FSM: Final State Machine
API: Application Programming Interface

B Complementary figures

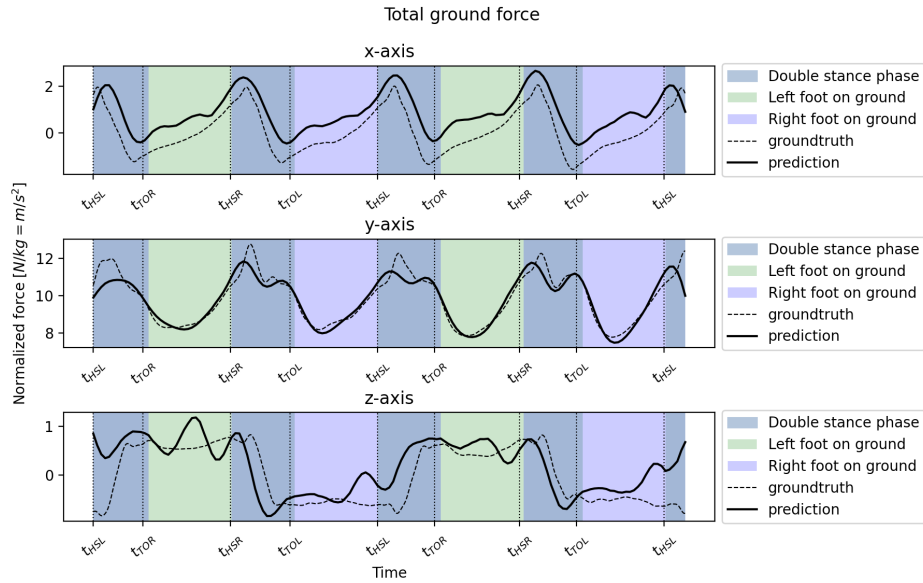


Figure 22: Graphical representation of the total ground reaction forces (predicted and experimental). Predicted GRF are similar for all implemented models using Opensim's method.

B COMPLEMENTARY FIGURES

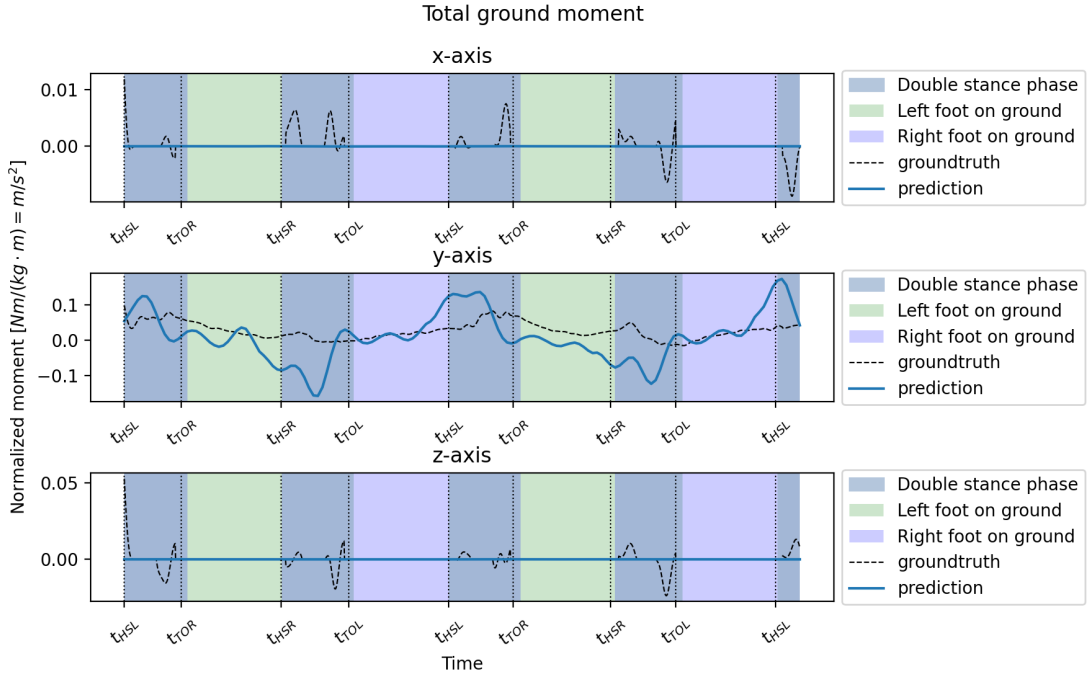


Figure 23: Graphical representation of the total ground reaction moments (predicted and experimental). Predicted GRM are similar for all implemented models using Opensim's method.

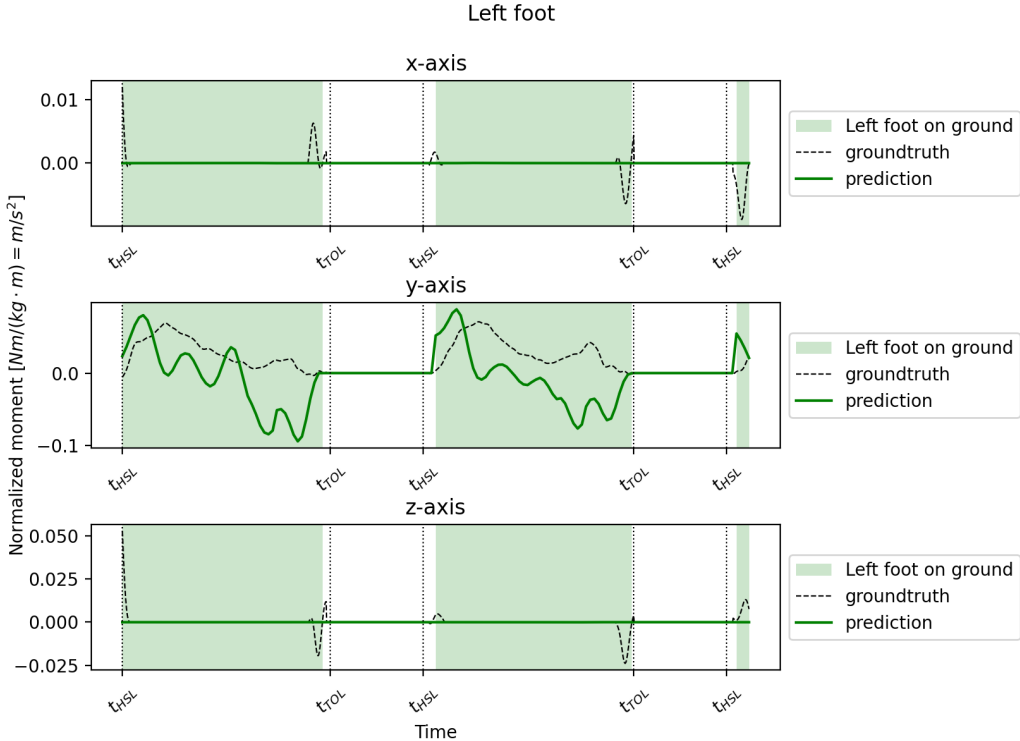


Figure 24: Graphical representation of the ground reaction moments (predicted and experimental) for the left leg on model 1 described in section 3.3.1.

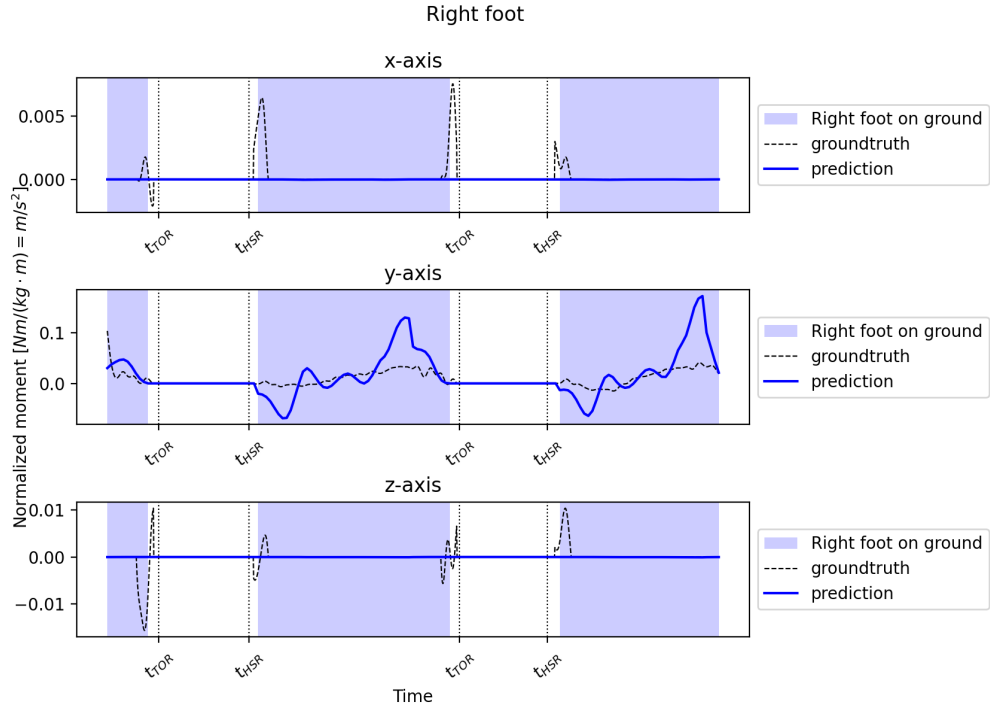


Figure 25: Graphical representation of the ground reaction moments (predicted and experimental) for the right leg on model 1 described in section 3.3.1.

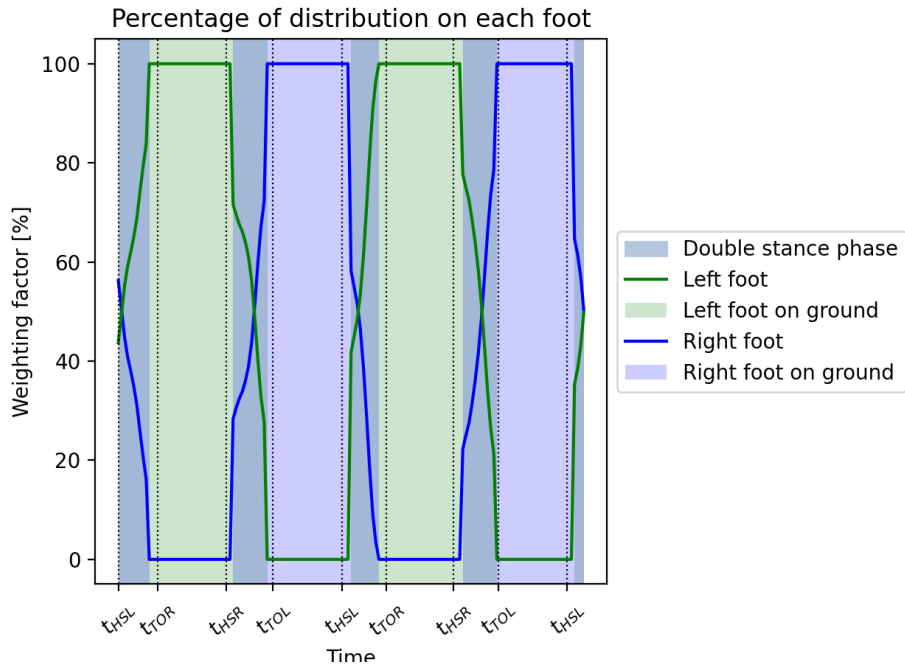


Figure 26: Representation of the distribution factors between the two legs for the model 1 described in section 3.3.1.

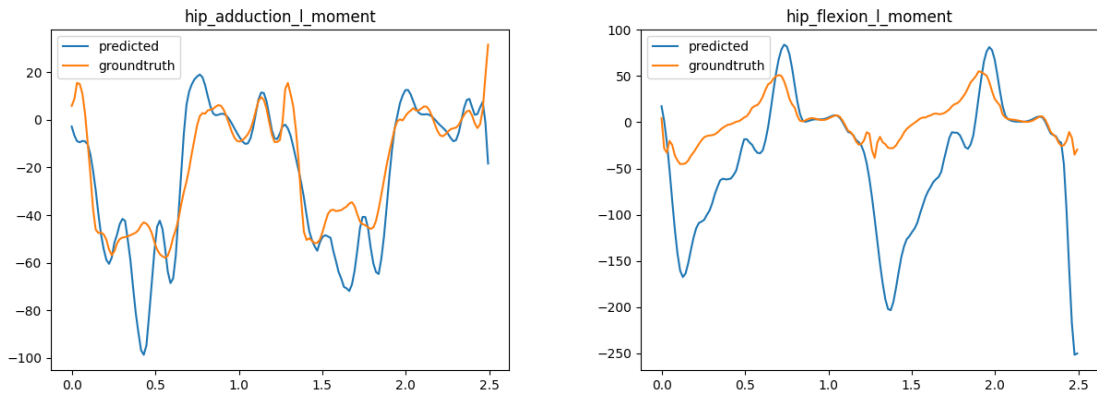


Figure 27: Inverse dynamics (moments) for hip adduction and flexion of the left foot.

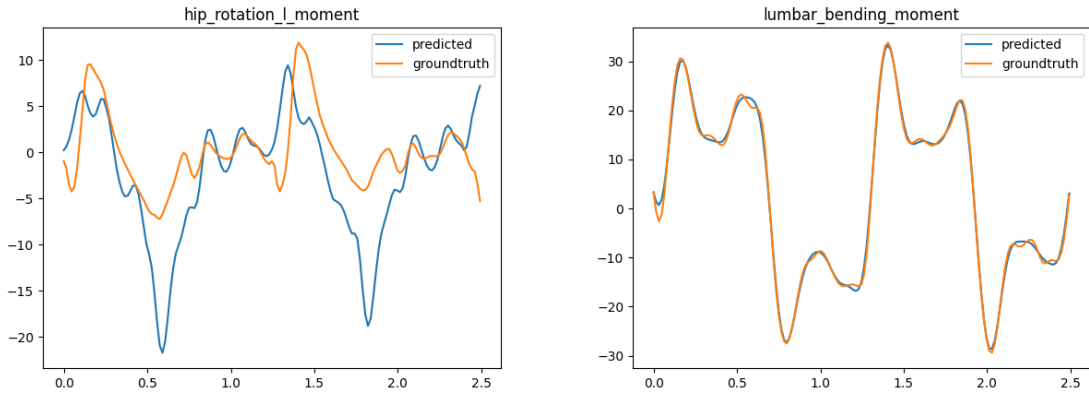


Figure 28: Inverse dynamics (moments) for hip rotation of the left foot and lumbar bending.

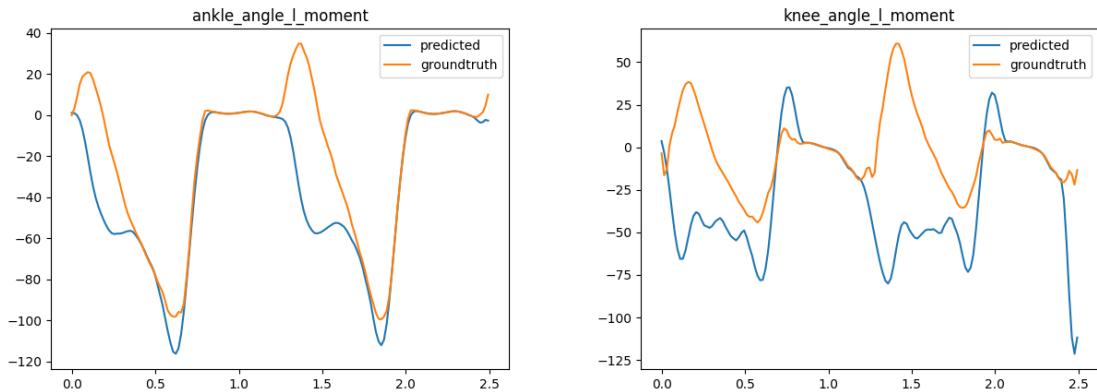


Figure 29: Inverse dynamics (moments) for ankle angle and knee angle of the left foot.

References

- [1] S. Skals supervised by M. S. Andersen and M. N. Castro : Master thesis about Prediction of ground reaction forces and moments during sports-related movements (2015).
- [2] S. Skals, M. K. Jung, M. Damsgaard, M. S. Andersen: Prediction of ground reaction forces and moments during sports-related movements. Springer Science+Business 39:175-195 (2016).
- [3] J. Rasmussen, M. de Zee, M. Damsgaard, S. T. Christensen, C. Marek and K. Siebertz: A General Method for Scaling Musculo-Skeletal Models. Computer Science (2005).
- [4] D. Krüger, S. Wartzack: A contact model to simulate human-artifact interaction based on force optimization: implementation and application to the analysis of a training machine. Taylor and Francis (2017).
- [5] H. X. Ryu, S. Park: Estimation of unmeasrud ground reaction force data based on the oscillatory characteristics of the center of mass during human walking. Journal of biomechanics (2018).
- [6] T. Geijtenbeek, A. J. van den Bogert, B. J. H. van Basten, A. Egges: Evaluating the Physical Realism of Character Animations Using Musculoskeletal Models. Springer-Verlag (2010).
- [7] A. Karatsidis: Kinetic Gait Analysis Using Inertial Motion Capture, *New Tools for Knee Osteoarthritis*. Doctoral thesis (2018).
- [8] Ren, L., Jones, R.K., Howard, D.: Whole body inverse dynamics over a complete gait cycle based only on measured kinematics. Journal of Biomechanics 41(12), 2750–2759 (2008). doi:10.1016/j.jbiomech.2008.06.001
- [9] Delp, S.L., Loan, J.P., Hoy, M.G., Zajac, F.E., Topp E.L., Rosen, J.M.: An interactive graphics-based model of the lower extremity to study orthopaedic surgical procedures, IEEE Transactions on Biomedical Engineering, vol. 37, pp. 757-767, 1990.
- [10] Yamaguchi G.T., Zajac F.E.: A planar model of the knee joint to characterize the knee extensor mechanism." J . Biomedcl7. vol. 21. pp. 1-10. 1989.
- [11] Anderson F.C., Pandy M.G.: A dynamic optimization solution for vertical jumping in three dimensions. Computer Methods in Biomechanics and Biomedical Engineering 2:201-231, 1999.
- [12] Anderson F.C., Pandy M.G.: Dynamic optimization of human walking. Journal of Biomechanical Engineering 123:381-390, 2001
- [13] Fluit R., Andersen M.S., Kolk S., Verdonschot N., Koopman H.F.J.M.: Prediction of ground reaction forces and moments during various activities of daily living. Journal of Biomechanics 47 p.2321–2329, 2014.